Constructing BiVO$_4$-Au@CdS photocatalyst with energic charge-carrier-separation capacity derived from facet induction and Z-scheme bridge for degradation of organic pollutants

Fei Ye[a,1], Houfen Li[b,1], Hongtao Yu[a], Shuo Chen[a], Xie Quan[a,*]

[a] Key Laboratory of Industrial Ecology and Environmental Engineering (Ministry of Education, China), School of Environmental Science and Technology, Dalian University of Technology, Dalian 116024, China
[b] College of Environmental Science and Engineering, Taiyuan University of Technology, Taiyuan, 030024, China

ARTICLE INFO

ABSTRACT

A rational design and precise control over charge carriers transportation in Z-scheme system is favorable for achieving its optimal photocatalytic performance. Herein, a ternary composite Z-scheme photocatalyst with Au@CdS selectively deposited on the {010} facets of BiVO$_4$ was prepared. Due to the fact that the CB edge and VB edge of the {110} facet of BiVO$_4$ are higher than those of its {010} facet, the photo-generated electrons and holes in well-faceted BiVO$_4$ transferred to the {010} and {110} facets, respectively. The electrons on the {010} facets of BiVO$_4$ transferred through Au NPs as the electron mediator to combine with holes of CdS at the interface. Benefiting from the dual-facilitated charge carriers transportation in Z-scheme and well-faceted BiVO$_4$ crystals, the photocatalytic efficiency of the optimal ternary BiVO$_4$-Au@CdS hybrids is 6.11, 3.03 and 2.95 times higher than those of BiVO$_4$, BiVO$_4$-Au and BiVO$_4$-CdS toward Rhodamine B degradation and 1.46 times higher than that of BiVO$_4$ (random facets)-Au@CdS toward 4-nonylphenol degradation. This work provides a new insight on rational design of Z-scheme system based on well-faceted nanocrystals for enhancing photocatalytic performance.

1. Introduction

As is well known, the photocatalytic activity can be improved by promoting the photo-generated electron-hole separation of photocatalysts. Nowadays, constructing Z-scheme photocatalysts [1–6] and synthesizing well-faceted crystal photocatalysts [7–11] are two of the common used strategies to achieve efficient charge carriers separation. A Z-scheme photocatalyst usually contains photosystem I (PS I), photosystem II (PS II) and an electron mediator [1,12–14]. During photocatalytic process, the photo-generated electrons of PS II transfer through electron mediator to recombine with the photo-generated holes of PS I at the interface, leaving electrons with higher reductive ability in PS I and holes with higher oxidative ability in PS II which can degrade organic pollutants [15–18]. This charge transfer route makes Z-scheme photocatalytic system not only promote photo-generated charge carriers separation but also keep their original redox capacities. A well-faceted crystal photocatalyst with various crystal facets exposed also makes efficient carriers separation. It is because electronic arrangement and energy band levels of each facet are different [19–22], which drives

electrons and holes to different facets. A typical example of a PS II semiconductor with facet effect is BiVO$_4$ [17,23,24]. Recent work confirmed that the CB edge and VB edge of the {110} facets of BiVO$_4$ are 0.42 and 0.37 eV higher than those of its {010} facets [8], which led to respective accumulation of electrons and holes at the {010} facets and the {110} facets, and achieved efficient spatial isolation.

These two properties hint it will be an efficient way to enhance the separation efficiency of photo-generated charge carriers via combining Z-scheme with facet effect, such as selectively depositing PS I on the electrons accumulated facet of PS II. To the best of our knowledge, very limited attention has been paid to study the performance discrepancy of Z-scheme constructed on different crystal facets.

Herein, taking BiVO$_4$ and Au@CdS as a proof-of-concept, we first design two types of ternary composite Z-scheme photocatalyst by selectively deposited Au@CdS on the {010} facet and randomly deposited Au@CdS on both {010} and {110} facets of BiVO$_4$, respectively. The elaborate design of ternary BiVO$_4$-Au@CdS Z-scheme photocatalysts was based on the following two aspects. On one hand, the efficient electrons and holes separation between {010} and {110} facets of

---

$BiVO_4$ ensure more electrons transfer to Au NPs (on the {010} facet of $BiVO_4$), which is the origin of performance discrepancy between these two Z-scheme photocatalysts. On the other hand, Au NPs play not only an electron mediator to facilitate the electrons of $BiVO_4$ recombine with the holes of CdS, but also an anchor for CdS to deposit on the surface of Au NPs owing to the existence of strong affinity between Au atoms and S atoms [25]. Based on above analysis, the selectively prepared $BiVO_4$-Au@CdS Z-scheme photocatalyst was expected to exhibit more efficient charge carriers separation ability and higher photocatalytic capacity than the randomly prepared one. To test the photocatalytic properties of as-prepared samples, the degradation of Rhodamine B (RhB) and 4-nonylphenol (4-NP) was conducted as probe reactions.

2. Experimental section

2.1. Preparation of catalysts

2.1.1. Synthesis of BiVO₄

$BiVO_4$ was synthesized by a hydrothermal process according to previously published procedures [8,26]. In brief, NH_4VO_3 (36.0 mmol) and $Bi(NO_3)_3 \cdot 5H_2O$ (36.0 mmol) were dissolved in 220 and 80 mL of 2.0 M nitric acid solutions, respectively. Then, the pH value of the resulting solution was adjusted to 2.0 with ammonia solution, after constant stirring and then aged for 2 h, the orange precipitate was transferred to a 100 mL Teflon-lined autoclave and heated at 200 °C for 24 h.

2.1.2. Synthesis of BiVO₄-Au

For the preparation of Au NPs selectively deposited on the {010} facets of $BiVO_4$, a photo-reduction method was employed. Typically, 200 mg of $BiVO_4$ was dispersed in 50 mL of deionized water, followed by addition of 0.5 mL $HAuCl_4$ aqueous solution (10 mM) (~0.5 wt% of Au/$BiVO_4$). The resulted suspension was irradiated under a 500 W Xe lamp (Zolix LSP-X500, Beijing Zhuolihanguang) with a 420 nm filter for 1 h, 2 h and 3 h. And the as-prepared catalysts were denoted as $BiVO_4$-Au-1, $BiVO_4$-Au-2 and $BiVO_4$-Au-3, respectively, according to the deposition time For the synthesis of Au NPs randomly deposited on the surface of $BiVO_4$ (c-$BiVO_4$-Au-2), a chemical reduction method was introduced. First, $HAuCl_4$ aqueous solution (0.5 mL, 10 mM) was added in deionized water (50 mL, pH was adjusted to 1 with hydrochloric acid) in the presence of $BiVO_4$ (200 mg), $NaBH_4$ solution (10 mL, 0.01 M) as reductant was then added into the suspension in an ice water bath under magnetic stirring. The reaction lasted for 2 h. All products were collected by filtration, and then washed and dried.

2.1.3. Synthesis of BiVO₄-Au@CdS

The CdS layer was coated on the Au NPs surface of $BiVO_4$-Au by a photo-deposition method. In a typical procedure, 50 mg of $BiVO_4$-Au, 247 mg of $Cd(NO_3)_2 \cdot 4H_2O$ and 8.4 mg of sulfur powder (S_8) were dispersed in 50 mL 10% ethanol aqueous to form a stable suspension and stirred for 30 min in the dark, followed by irradiated with light for 2 h. By using $BiVO_4$-Au-1, $BiVO_4$-Au-2 and $BiVO_4$-Au-3 as the precursor, respectively, the obtained $BiVO_4$-Au@CdS was named as $BiVO_4$-Au@CdS-1, $BiVO_4$-Au@CdS-2 and $BiVO_4$-Au@CdS-3, respectively. By using c-$BiVO_4$-Au-2 as the precursor, the obtained $BiVO_4$-Au@CdS was named as c-$BiVO_4$-Au@CdS-2.

2.1.4. Synthesis of BiVO₄-CdS

50 mg of $BiVO_4$, 247 mg of $Cd(NO_3)_2 \cdot 4H_2O$ and 8.4 mg of S_8 were dispersed in 50 mL 10% ethanol aqueous to form a stable suspension and stirred for 30 min in the dark, followed by irradiated with light for 2 h.

2.2. Characterization

The morphologies and microstructures of the samples were characterized by a field emission scanning electron microscope (SEM,

Hitachi S4800) and a transmission electron microscope (TEM, FEI-Tecnai G^2 F30). The chemical composition was investigated by the energy dispersive X-ray spectroscopy (EDS, 550i, IXRF Systems). The crystal structures were investigated using an X-ray diffractometer (XRD, EMPYREAN, PANalytical) with Co kα radiation (λ = 0.179 nm) and the element states of the samples were analyzed by an X-ray photoelectron spectrometer (XPS, ESCALAB 250XI, Thermo Fisher Scientific) with a Al kα source (1486.6 eV). The element content was measured by an inductively coupled plasma atomic emission spectrometer (ICP-AES) performed on a Perinlmer Optima 2000DV instrument. UV–vis diffuse reflectance spectra (DRS) of the powders were recorded on a Shimadzu UV-2450 spectrophotometer. Photoluminescence (PL) spectra of the samples were measured using a fluorescence spectrometer (Hitachi F-4500). The RhB degradation products were determined by liquid chromatography-Triple Quadrupole mass spectrometer (Agilent 1100-6410). An electron spin resonance (ESR) spectrometer (A200, Bruker) was employed to detect superoxide radicals ($\cdot O_2^-$) and hydroxyl radicals ($\cdot OH$) in methanol solution and aqueous solution, respectively, with 5,5-dimethy l-L-pyrroline-n-oxide (DMPO, 50 mM) as a spin trap to stabilize the radicals.

2.3. Photocurrent measurements

The photocurrent density of the samples was measured on an electrochemical workstation (CHI 660D, Shanghai Chenhua Instrument Co), using a three-electrode mode in 0.1 M Na_2SO_4, with prepared samples electrophoresis deposition to conductive glass as the working electrode, Ag–AgCl electrode as the reference electrode and platinum sheet as the counter electrode, respectively. The working electrode was used as the anode for the electrochemical characterization with a bias voltage of +0.5 V. A 500 W xenon arc lamp (Zolix LSP-X500, Beijing Zhuolihanguang) was used as light source with a visible light cut-off filter (λ > 420 nm), and the incident light intensity was 100 mW cm^{-2}.

2.4. Photocatalytic reactions

Photocatalytic degradation processes of Rhodamine B (RhB) and 4-nonylphenol (4-NP) on as-prepared photocatalysts were performed to evaluate their photocatalytic capabilities. Before the photocatalytic process, 20 mg photocatalyst was added to a 20 mL RhB solution (5 mg L^{-1}) and the mixture was stirred in the dark for 30 min to ensure adsorption equilibrium. The RhB concentration was determined by a UV–vis spectrophotometer (JASCO V550). The 4-NP degradation test was carried out under the same light irradiation, with 10 mg photocatalyst added to the 20 mL 4-NP solution (2×10^{-4} M), and the mixture was stirred in dark for 30 min to ensure adsorption equilibrium. The 4-NP concentration was determined by high-performance liquid chromatography with a multi-wavelength fluorescence detector (Waters 2475). The mobile phase was acetonitrile/water containing 0.1% trifluoroacetic acid at a flow rate of 1.0 cm^3 min^{-1}, and the excitation and detection wavelengths were set at 270 and 320 nm, respectively [27].

3. Results and discussions

The two-step photo-reduction process for synthesizing the ternary composite Z-scheme photocatalyst with core-shell structured Au@CdS NPs selectively deposited onto the {010} facets of $BiVO_4$ was illustrated in Scheme 1. As shown in Scheme 1, during the first photo-reduction process, owing to the existence of energy level discrepancy between {010} and {110} facets of $BiVO_4$ crystals [8], the photo-generated electrons transferred to the {010} facets and holes to the {110} facets, respectively. This property provides a precondition to selectively reduce Au^{3+} to Au NPs on the {010} facets of $BiVO_4$ crystals. Then, during the second photo-reduction process, benefitting from their good
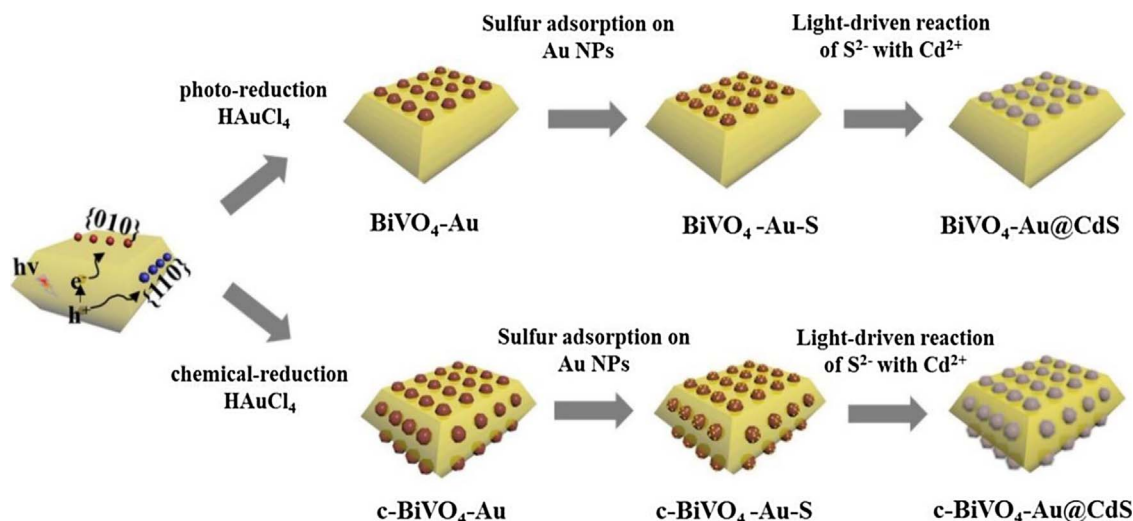
Scheme 1. Schematic illustration for preparation of ternary BiVO₄-Au@CdS Z-scheme photocatalytst.

affinity with Au atoms, S_8 molecules preferred to adsorb on the surface of Au atoms and can be reduced by the photo-generated electrons. Meanwhile, S^{2-} ions were released and reacted with Cd^{2+} to form CdS shell on the surface of Au NPs [28]. By tuning the deposition time of Au nanoparticles for 1 h, 2 h and 3 h, we can obtain a series of samples (BiVO₄-Au-1, 2 and 3) with different Au NPs loading amounts. By depositing CdS on BiVO₄-Au-1, BiVO₄-Au-2 and BiVO₄-Au-3, respectively, we further obtained BiVO₄-Au@CdS-1, BiVO₄-Au@CdS-2 and BiVO₄-Au@CdS-3, respectively. The contents of Au and CdS were measured by ICP-AES (Table S1), there was an increased trend with longer deposition time.

Taking BiVO₄-Au@CdS-2 as an example, the proprieties of the samples (including binary BiVO₄-Au-2 and ternary BiVO₄-Au@CdS-2) obtained during the photo-reduction process were investigated. The morphology of as-prepared samples was characterized by SEM. As shown in Fig. 1a, the as-prepared BiVO₄ was regularly shaped sample of truncated bipyramid with smooth top/down surface of {010} facets and side surface of {110} facets being exposed. After the first photo-reduction step, many Au NPs with diameter about 25 nm (Fig. S1) were deposited on the {010} facets of BiVO₄ crystals, while the {110} facets had no Au NPs deposition and remained smooth (Fig. 1b). Its preferential deposition on the {010} facets is ascribed to that photo-generated electrons accumulated on the {010} facets of BiVO₄ crystals, where Au^{3+} could get electrons and be reduced to Au NPs. Fig. 1c shows the SEM image of BiVO₄-Au@CdS, after the second photo-reduction step, the size of Au@CdS NPs on the {010} facets of BiVO₄ grew larger than Au NPs in the first step, reaching to about 37 nm (Fig. S1). This result hinted that CdS can be deposited on the surface of Au NPs. Fig. 1d shows the SEM image of BiVO₄-CdS, where CdS also selectively deposited on the {010} facets of BiVO₄. XRD patterns in Fig. S2 revealed that the BiVO₄-Au@CdS patterns are agreement with those of BiVO₄, indicating the introduction of Au@CdS NPs did not change the crystal phase and crystallinity of BiVO₄. However, no diffraction peaks at 38.2° and 26.5° corresponding to Au (111) and CdS (002) were detected in the XRD patterns of either sample, which was ascribed to the low loading amounts [23,29] (Fig. S2). Therefore, the existence of Au@CdS NPs was further investigated by other approaches, including EDS and TEM.

The EDS elements mapping (Fig. S3) revealed the Au, Cd and S elements distributed sporadically over the selected region on {010} facets of BiVO₄ crystals, indicating the existence of Au and CdS. As shown in Fig. 1e, the lattice fringe spacing about 0.235 nm can be clearly observed, which is in accordance with {111} planes of Au NPs. And after deposition of CdS on Au, the Au@CdS can be observed clearly (Fig. 1f), as the shell has a lattice fringe spacing about 0.34 nm

corresponding to the {111} planes of CdS [30]. These results along with the SEM analysis could demonstrate that the ternary BiVO₄-Au@CdS photocatalyst was successfully synthesized by the step-by-step photo-reduction procedures.

To further confirm the existence of Au@CdS in the system, XPS analysis was conducted. Fig. 2a shows the XPS survey spectrum for BiVO₄-Au@CdS-2, confirming the presence of Bi, V, O, Au, Cd and S elements in the sample. The chemical valence state of Au, Cd, and S elements was further characterized by high-resolution XPS analysis. As shown in Fig. 2b, the high-resolution XPS spectrum of Au 4f displayed doublet peaks located at 83.95 and 87.7 eV, corresponding to Au $4f_{7/2}$ and Au $4f_{5/2}$ of metallic Au [31,32]. The intensity of Au 4f peaks in BiVO₄-Au@CdS-2 was much weaker than those in BiVO₄-Au-2, which might arise from the fact that Au NPs were covered by CdS in the former [28]. From Fig. 2c, the high-resolution XPS spectrum shows that the binding energy of Cd $3d_{5/2}$ and Cd $3d_{3/2}$ in the ternary composite photocatalyst were 405.25 and 412.0 eV, corresponding to $3d_{5/2}$ and $3d_{3/2}$ of Cd^{2+} in CdS, respectively [33]. However, the peaks of S 2p spectrum located at about 160 eV cannot be found, owing to its being covered by the strong Bi 4f peaks closed to them (Fig. S4) [23].

To investigate the optical properties of the obtained samples, UV–vis diffuse reflectance spectra of BiVO₄, BiVO₄-Au-2, BiVO₄-Au@CdS and BiVO₄-CdS were measured. As shown in Fig. 3a, it is easy to see that BiVO₄ exhibited the inherent visible light absorption with absorption edge at about 520 nm. Compared to BiVO₄, BiVO₄-Au-2 exhibited a broader absorption peak around 620 nm, which was attributed to the surface plasmon resonance (SPR) absorption of Au NPs [34]. BiVO₄-CdS extended the optical absorption edge from 520 nm to about 550 nm after depositing CdS on the surface of BiVO₄. As for BiVO₄-Au@CdS, all of the three samples (BiVO₄-Au@CdS-1, 2, 3) showed a broader visible light absorption and enhanced absorption intensity than BiVO₄, BiVO₄-Au-2 and BiVO₄-CdS, which might derive from the co-effect of intimate contacted Au and CdS [35]. The photoluminescence spectrum (PL) and photocurrent density were commonly used to evaluate the ability of charge carriers production and separation in photocatalysts. From Fig. 3b, it can be seen that the PL spectrum of BiVO₄ exhibited the strongest photoluminescence intensity, indicating its high photo-generated electron-hole recombination efficiency regardless of the existence of facet-induction charge carriers separation between different facets of BiVO₄, while other samples exhibited weaker PL intensities, meaning that the photo-generated electron-hole recombination can be effectively alleviated through constructing heterostructure. Among them, BiVO₄-Au-2 had a weaker PL intensity than BiVO₄-CdS, suggesting that the barrier of charge carriers transfer might be lower for BiVO₄-Au-2 than that of BiVO₄-CdS heterostructure. The
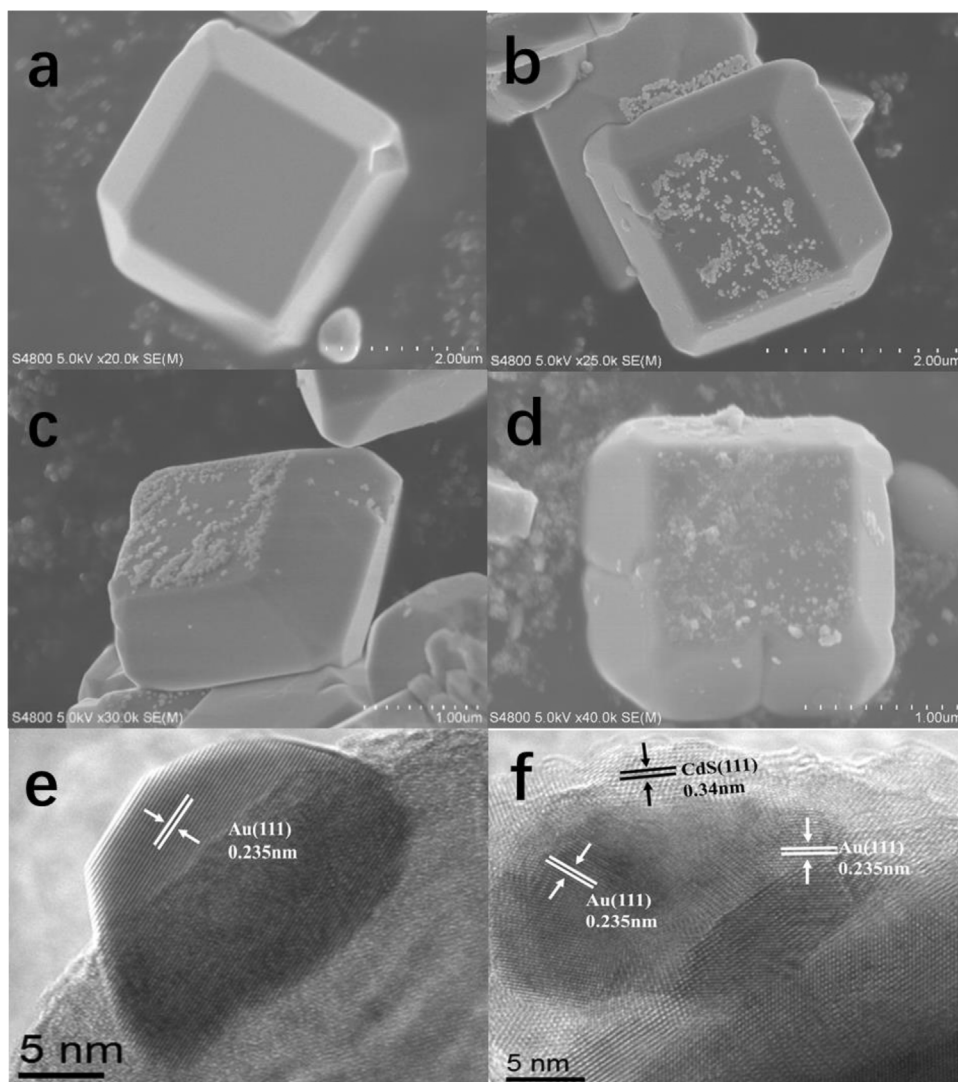
Fig. 1. SEM images of (a) BiVO$_4$, (b) BiVO$_4$-Au-2, (c) BiVO$_4$-Au@CdS-2 and (d) BiVO$_4$-CdS, (e) HRTEM image of BiVO$_4$-Au-2 and (f) BiVO$_4$-Au@CdS-2.

even weaker photoluminescence intensity, indicating more efficient charge carriers separation, was observed on the BiVO$_4$-Au@CdS. The PL spectra intensity of all BiVO$_4$-Au@CdS samples (BiVO$_4$-Au@CdS-1, 2 and 3) were lower than that of BiVO$_4$, BiVO$_4$-Au-2 and BiVO$_4$-CdS, which were attributed to the most suppressed electron-hole recombination process. Moreover, the result of photocurrent measurement was in agreement with the above results, following the order of BiVO$_4$-Au@CdS > BiVO$_4$-Au-2 > BiVO$_4$-CdS > BiVO$_4$. For BiVO$_4$-Au-2, the photocurrent density increased owing to more efficient electrons transfer from BiVO$_4$ to Au NPs, which further benefited the charge carriers separation. As for BiVO$_4$-CdS, in spite of the presence of heterostructure between CdS NPs and BiVO$_4$, the poor interfacial electrons transfer kinetics due to lacking of electron mediator was unfavorable for the charge carriers separation of BiVO$_4$-CdS, therefore the photocurrent density increase than that of BiVO$_4$ was slightly. Notably, in the samples BiVO$_4$-Au@CdS-1, 2 and 3, introducing Au NPs as a mediator can promote the electrons transfer from BiVO$_4$ to CdS through a Z-scheme mechanism, which was in accordance with the facet-induction charge carriers transfer effect and lead to a further increased photocurrent response. Among all the three samples of BiVO$_4$-Au@CdS, the photocurrent density of BiVO$_4$-Au@CdS-2 was higher than that of BiVO$_4$-Au@CdS-1 and BiVO$_4$-Au@CdS-3, which means that the contents of Au NPs should be considered to obtain optimal photocatalytic performance. Au NPs with relatively low content (BiVO$_4$-Au@CdS-1) was not enough to promote the charge carriers separation, on the other

hand, Au NPs with relatively high content (BiVO$_4$-Au@CdS-3) can serve as charge carriers recombination centers and facilitate the recombination of electron-hole pairs generated from BiVO$_4$, thus the optimal photocatalytic performance was obtained with BiVO$_4$-Au-CdS-2.

In order to evaluate the photocatalytic performance of as-prepared samples, degradation of RhB, a typical organic dye, was conducted under visible light irradiation and the results are shown in Fig. 4a, b. It can be observed that the concentration of RhB exhibited almost no change without the addition of any photocatalyst, indicating the photolysis of RhB was negligible. Compared with the pristine BiVO$_4$, all the other samples (BiVO$_4$-Au-2, BiVO$_4$-CdS and BiVO$_4$-Au@CdS) exhibited a gradually increased RhB degradation percent, which arose from the enhanced photo-generated charge carriers separation capacities of BiVO$_4$ in the multi-composite photocatalysts. Furthermore, BiVO$_4$-Au@CdS-2 displayed the highest kinetic rate constant (0.0130 min^{-1}), which is 6.11, 3.03 and 2.95 times higher than those of BiVO$_4$ (0.0021 min^{-1}), BiVO$_4$-Au-2 (0.0043 min^{-1}) and BiVO$_4$-CdS (0.0044 min^{-1}) counterparts. The optimal photocatalytic ability of BiVO$_4$-Au@CdS-2 can be attributed to its higher charge carriers separation efficiency and stronger redox ability (this will be discussed later), which is in accordance with the results of photocurrent density and photoluminescence tests. The intermediate products of RhB degradation were detected by LC–MS, and the results in Fig. S5 showed five intermediate products namely *N, N*-diethyl-*N'*-ethylrhodamine (DER), *N, N*-diethylrhodamine (DR), *N*-ethyl-*N'*-ethylrhodamine (EER),
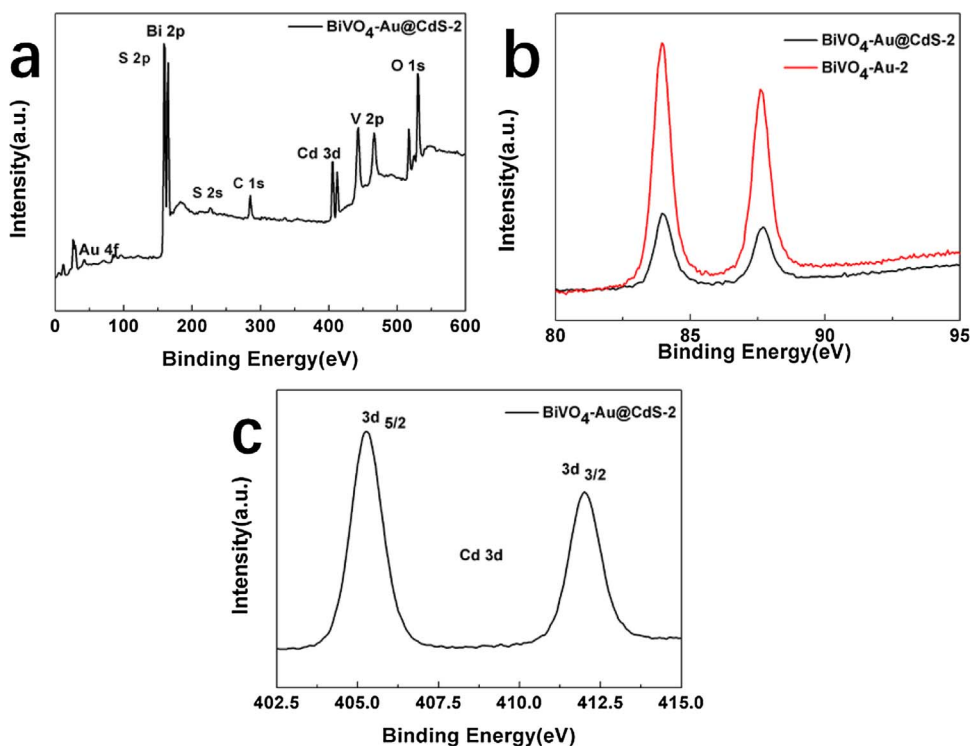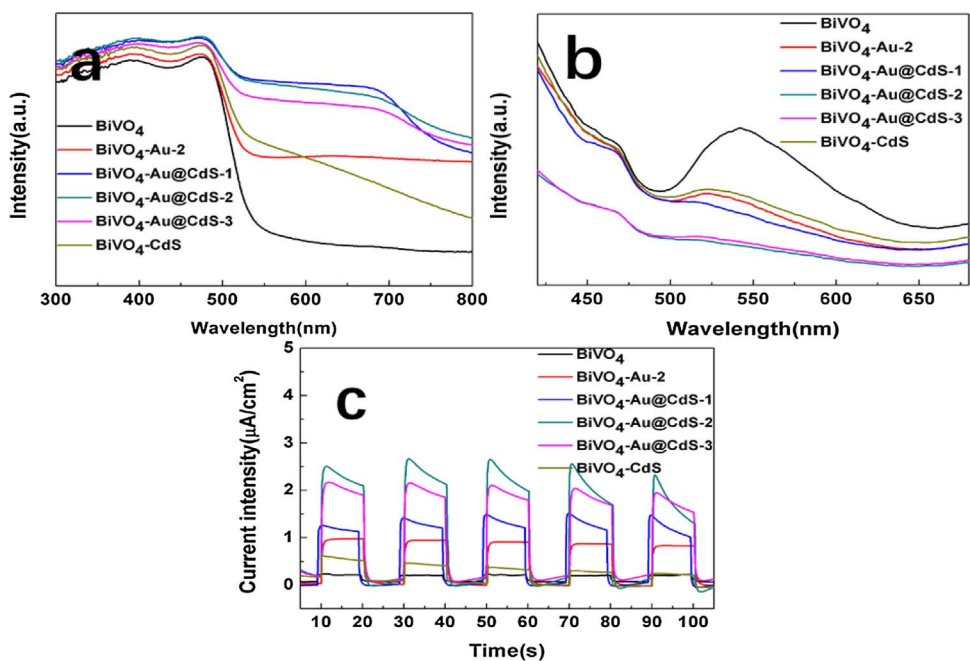
N-ethylrhodamine (ER), and Rhodamine (R) was detected, which indicated RhB was degraded by de-ethylation gradually. The concentration of the intermediate products reached to their maximum at 1 h, and then was almost deminished after 3 h. This also provides evidence that the RhB could be decomposed completely.

To further evaluate the photocatalytic activity of ternary composites photocatalyst (BiVO$_4$-Au@CdS), here, we chose 4-NP as another model contaminant to degrade and the results are shown in Fig. 5a, b. As expected, the photocatalytic degradation performance showed a similarity trend with that of RhB degradation (Fig. 5a). As shown in Fig. 5b, the degradation kinetic rates followed this order: BiVO$_4$-Au@CdS-2 (0.0430 min^{-1}) > BiVO$_4$-Au-2 (0.0336 min^{-1})

> BiVO$_4$-CdS (0.0249 min^{-1}) > BiVO$_4$ (0.0175 min^{-1}). This result further confirmed the deposition of both Au and CdS NPs endowed the ternary BiVO$_4$-Au@CdS composites with enhanced photocatalytic performance, which was probably originated from the aforementioned Z-scheme mechanism. Through this mechanism not only the photo-generated charge carriers separation efficiency was enhanced, but the strong redox ability was also retained. Finally, the stability of BiVO$_4$-Au@CdS-2 was tested by the cyclic photocatalytic degradation of 4-NP (Fig. 5c). During the four consecutive cycles, no obvious loss of photocatalytic activity was observed, which indicated it is photostable.

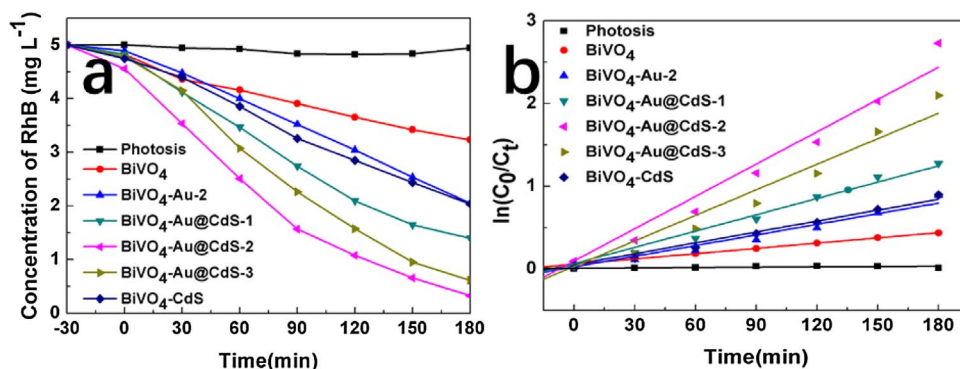To verify the aforementioned charge carriers transfer mechanism

Fig. 4. (a) Concentration of RhB versus time plots and (b) degradation kinetics of RhB during the photocatalytic process on different photocatalysts under visible light irradiation ($\lambda \geq 420\,nm$).
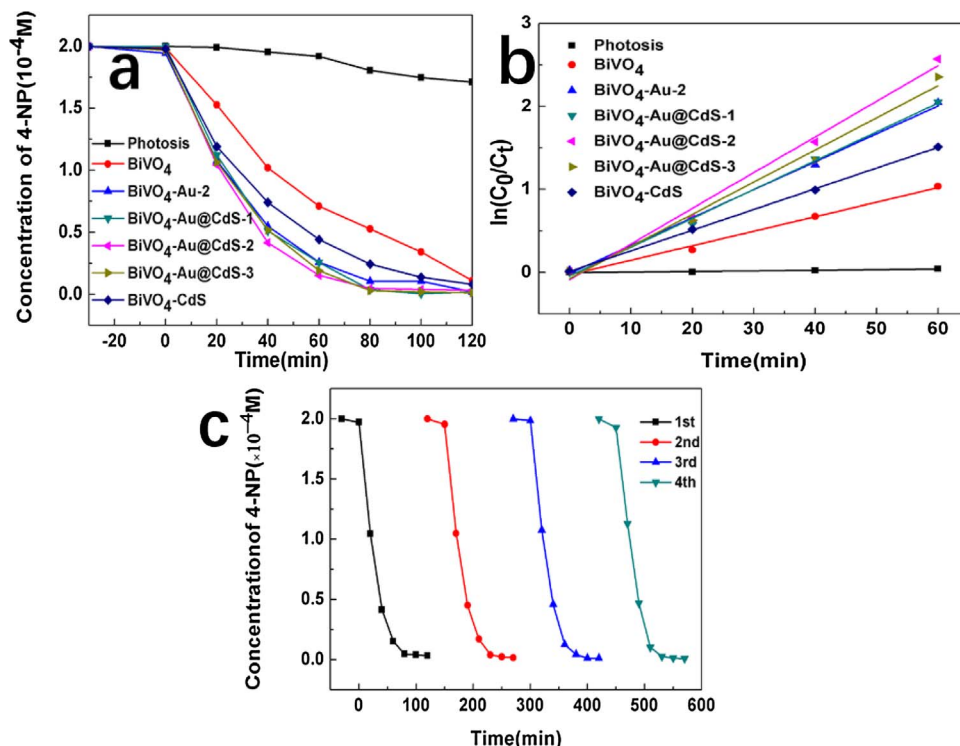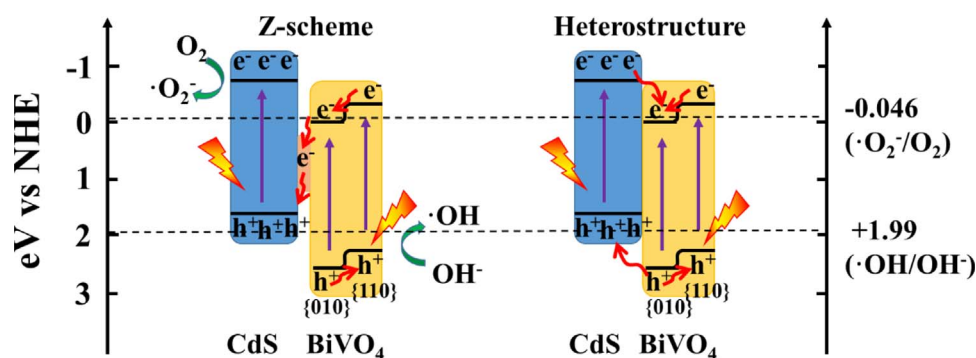

Fig. 5. (a) Concentration of 4-NP versus time plots, (b) degradation kinetics of 4-NP during the photocatalytic process on different photocatalysts under visible light irradiation ($\lambda \geq 420\,nm$) and (c) the stability test of the BiVO$_4$-Au@CdS-2 photocatalyst in the recycling reactions for the degradation of 4-NP.

(Z-scheme mechanism), we employed ESR spin-trapping to detect the transient radical intermediates. According to the energy band alignments in Scheme 2, the energy levels of electrons on the conduction band of CdS are sufficient negative to reduce O$_2$ into $\cdot$O$_2^-$ radical (E^0 (O$_2$/$\cdot$O$_2^-$) = -0.046 V vs NHE [36]) and the energy levels of holes on the valence band of BiVO$_4$ are positive enough to oxide OH$^-$ into $\cdot$OH radical (E^0 ($\cdot$OH/OH$^-$) = 1.99 V vs NHE [36]), which indicated that through Z-scheme charge transfer mechanism the photocatalytic system can produce $\cdot$OH and $\cdot$O$_2^-$ radical simultaneously. The ESR results in Fig. 6a showed that the DMPO-$\cdot$OH adduct, four peaks with spectral line intensities of 1:2:2:1, was detected in all samples, this was due to that all the samples contained BiVO$_4$ and the holes in BiVO$_4$ accumulated to the {110} facet, which can oxide OH$^-$ into $\cdot$OH. The strongest signal intensity was observed in BiVO$_4$-Au@CdS-2, which indicated more holes were preserved through the Z-scheme mechanism. BiVO$_4$-CdS exhibited weaker signal intensity than that of BiVO$_4$-Au-2 due to that some holes transferred to the VB of CdS and lost the ability to produce $\cdot$OH radical, while the signal intensity of BiVO$_4$-CdS was still stronger than that of BiVO$_4$ owing to the formation of heterostructure between BiVO$_4$ and CdS, which promoted charge carriers separation and preserved more holes than BiVO$_4$. From Fig. 6b, it can be observed that the weak signal of DMPO-$\cdot$O$_2^-$ adduct with four characteristic peaks with the standard ratio of intensities 1:1:1:1 [37] was detected in

the BiVO$_4$-Au@CdS-2, further confirmed the Z-scheme charge transfer mechanism. On the other hand, the characteristic peaks of $\cdot$O$_2^-$ were not observed in other samples including BiVO$_4$, BiVO$_4$-Au-2 and BiVO$_4$-CdS photocatalysts, indicating that the electrons on the {110} facet and on the conduction band of CdS were transferred to the {010} facet of BiVO$_4$, and lost the ability to reduce O$_2$ into $\cdot$O$_2^-$ radical.

In order to further demonstrate the role of facet-induction charge carriers separation in achieving excellent activities of Z-scheme photocatalyst BiVO$_4$-Au@CdS, herein, the randomly deposited Au and Au@CdS NPs on both {010} and {110} facets of BiVO$_4$ crystals was prepared by a chemical reduction method as comparison. As shown in the SEM image (Fig. S6), the BiVO$_4$-Au prepared via chemical reduction (denoted as c-BiVO$_4$-Au) exhibited uniform distribution of Au NPs on the whole BiVO$_4$ crystal surface including {010} and {110} facets. ICP-AES analysis revealed the deposited Au NPs has a real loading percentage of approximately 0.4921 wt% for c-BiVO$_4$-Au and 0.4971 wt% for BiVO$_4$-Au (Table S2), which are comparable to the raw material ratio of 0.5 wt%. And after the deposition of CdS, the c-BiVO$_4$-Au@CdS had a coarser surface compared to that of c-BiVO$_4$-Au. Subsequently, the optical properties and the charge carrier separation properties of c-BiVO$_4$-Au@CdS were compared with those of BiVO$_4$-Au@CdS by analyzing their DRS, PL and photocurrent results. From Fig. 7a, it can be seen that the c-BiVO$_4$-Au exhibited stronger visible light absorption

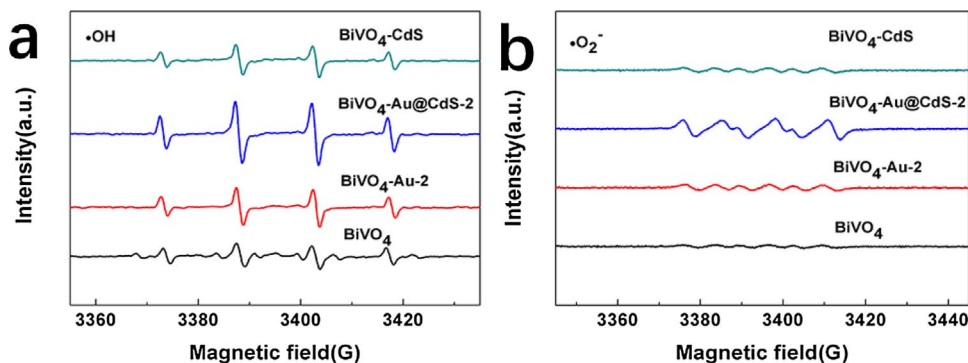**Scheme 2.** Proposed photocatalytic mechanisms of CdS-Au-BiVO₄ Z-scheme and CdS-BiVO₄ heterostructure.

Fig. 6. ESR signals of DMPO-·OH (a) and DMPO-·O₂⁻ (b) adducts after 5 min irradiation in the presence of different photocatalysts (λ ≥ 420 nm).
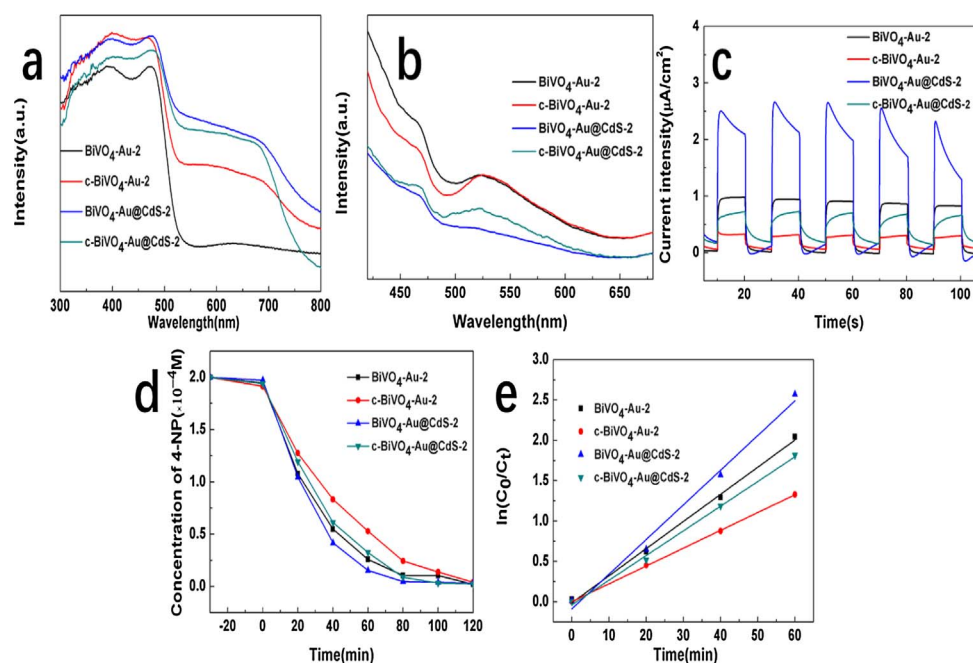

Fig. 7. (a) UV–vis absorption spectra, (b) photoluminescence spectra and (c) photocurrent response of BiVO₄-Au-2, c-BiVO₄-Au-2, BiVO₄-Au@CdS-2 and c-BiVO₄-Au@CdS-2, (d) concentration of 4-NP versus time plots and (e) degradation kinetics of 4-NP during the photocatalytic process on different photocatalysts under visible light irradiation (λ ≥ 420 nm).

than BiVO₄-Au owing to the improving surface plasmon resonance (SPR) absorption of Au NPs, while the light absorption intensity of c-BiVO₄-Au@CdS showed a similar trend with that of BiVO₄-Au@CdS when the Au NPs were covered by CdS NPs. Despite the similar light absorption properties, weaker PL intensity and higher photocurrent density were observed for BiVO₄-Au and BiVO₄-Au@CdS compared with those of c-BiVO₄-Au and c-BiVO₄-Au@CdS (Fig. 7b, c), indicating that the materials with selectively deposited Au NPs on the {010} facets of BiVO₄ possess more efficient charge carriers separation abilities than the non-selectively deposited ones. This is because the energy levels of {010} facet were lower than that of {110} facet of BiVO₄, therefore, photo-generated electrons transferred to and accumulated on the {010} facet, and photo-generated holes transferred to and accumulated on the {110} facet. As a result, in the selectively prepared samples (BiVO₄-Au, BiVO₄-Au@CdS), the accumulated electrons transferred favourably from the {010} facets to the Au NPs, which further promoted the electrons and holes separation. On the contrary, in the randomly prepared samples (c-BiVO₄-Au, c-BiVO₄-Au@CdS), a part of Au NPs were deposited on the hole-accumulated {110} facet, in which few electrons transferred from {110} facet to Au NPs, and accumulated photo-generated holes on the {110} facet were likely to recombine with the electrons on Au NPs, thus deteriorating its photocatalytic performance. The 4-NP degradation experiment was also conducted and the corresponding results were shown in Fig. 7d, e. The degradation kinetic rate

of BiVO$_4$-Au@CdS (0.0430 min^{-1}) is 1.46 times higher than that of c-BiVO$_4$-Au@CdS (0.0221 min^{-1}), which further confirmed the positive effect of facet-induction in promoting charge carriers separation.

4. Conclusion

A facet-related ternary composite Z-scheme photocatalyst was successfully prepared through a two-step photo-reduction process based on facet-induction charge carriers separation of BiVO$_4$ nanocrystals under visible-light irradiation. Compared to the pristine BiVO$_4$, BiVO$_4$-Au (with only Au NPs deposited), BiVO$_4$-CdS (with only CdS deposited) and c-BiVO$_4$-Au@CdS (with Au@CdS NPs no-selectively deposited), the well-designed BiVO$_4$-Au@CdS photocatalyst was demonstrated to exhibit higher photocatalytic organic pollution degradation performance, which can be attributed to the synergistic effect between facet induction effect of BiVO$_4$ and Z-scheme mechanism. On one hand, the facet-induction charge carriers separation facilitated the photo-generated electrons of BiVO$_4$ oriented accumulation on the {010} facets and then transferred through Au NPs to combine with holes in CdS shell, on the other hand, the Z-scheme mechanism reserved the strong redox ability of BiVO$_4$-Au@CdS. This work provides a new insight to rationally designing Z-scheme photocatalysts with specified crystal facets, which is of importance for photocatalysts with efficient charge separation and high photocatalytic performance.

Acknowledgements

Appendix A. Supplementary data

Supplementary data associated with this article can be found, in the online version, at https://doi.org/10.1016/j.apcatb.2017.12.020.

References

[1] H. Tada, T. Mitsui, T. Kiyonaga, T. Akita, K. Tanaka, All-solid-state Z-scheme in CdS-Au-TiO$_2$ three-component nanojunction system, Nat. Mater. 5 (2006) 782–786.
[2] H.J. Yun, H. Lee, N.D. Kim, D.M. Lee, S. Yu, J. Yi, A combination of two visible-light responsive photocatalysts for achieving the Z-scheme in the solid state, ACS Nano 5 (2011) 4084–4090.
[3] P. Zhou, J.G. Yu, M. Jaroniec, All-solid-state Z-scheme photocatalytic systems, Adv. Mater. 26 (2014) 4920–4935.
[4] T.M. Suzuki, A. Iwase, H. Tanaka, S. Sato, A. Kudo, T. Morikawa, Z-scheme water splitting under visible light irradiation over powdered metal-complex/semiconductor hybrid photocatalysts mediated by reduced graphene oxide, J. Mater. Chem. A 3 (2015) 13283–13290.
[5] A.Y. Meng, B.C. Zhu, B. Zhong, L.Y. Zhang, B. Cheng, Direct Z-scheme TiO$_2$/CdS hierarchical photocatalyst for enhanced photocatalytic H$_2$-production activity, Appl. Surf. Sci. 422 (2017) 518–527.
[6] T.M. Di, B.C. Zhu, B. Cheng, J.G. Yu, J.S. Xu, A direct Z-scheme g-C$_3$N$_4$/SnS$_2$ photocatalyst with superior visible-light CO$_2$ reduction performance, J. Catal. 352 (2017) 532–541.
[7] A.Y. Meng, J. Zhang, D.F. Xu, B. Cheng, J.G. Yu, Enhanced photocatalytic H$_2$-production activity of anatase TiO$_2$ nnanosheet by selectively depositing dual-cocatalysts on {101} and {001} facets, Appl. Catal. B 198 (2016) 286–294.
[8] R.G. Li, F.X. Zhang, D.G. Wang, J.X. Yang, M.R. Li, J. Zhu, X. Zhou, H.X. Han, C. Li, Spatial separation of photogenerated electrons and holes among {010} and {110} crystal facets of BiVO$_4$, Nat. Commun. 4 (2013) 1432.
[9] J. Ding, Y.Y. Chai, Q.Q. Liu, X. Liu, J. Ren, W.L. Dai, Selective deposition of silver nanoparticles onto WO$_3$ nanorods with different facets: the correlation of facet-induced electron transport preference and photocatalytic activity, J. Phys. Chem. C 120 (2016) 4345–4353.
[10] M.L. Huang, S.X. Weng, B. Wang, J. Hu, X.Z. Fu, P. Liu, Various facet tunable ZnO crystals by a scalable solvothermal synthesis and their facet-dependent photocatalytic activities, J. Phys. Chem. C 118 (2014) 25434–25440.
[11] J. Jiang, K. Zhao, X.Y. Xiao, L.Z. Zhang, Synthesis and facet-dependent photoreactivity of BiOCl single-crystalline nanosheets, J. Am. Chem. Soc. 134 (2012) 4473–4476.
[12] J.J. Li, Y.L. Xie, Y.J. Zhong, Y. Hu, Facile synthesis of Z-scheme Ag$_2$CO$_3$/Ag/AgBr ternary heterostructured nanorods with improved photostability and photoactivity, J. Mater. Chem. A 3 (2015) 5474–5481.
[13] A. Iwase, S. Yoshino, T. Takayama, Y.H. Ng, R. Amal, A. Kudo, Water splitting and CO$_2$ reduction under visible light irradiation using Z-scheme systems consisting of metal sulfides, CoOx-loaded BiVO$_4$, and a reduced graphene oxide electron mediator, J. Am. Chem. Soc. 138 (2016) 10260–10264.
[14] M. Wang, Q.T. Han, L. Li, L.Q. Tang, H.J. Li, Y. Zhou, Z.G. Zou, Construction of an all-solid-state artificial Z-scheme system consisting of Bi$_2$WO$_6$/Au/CdS nanostructure for photocatalytic CO$_2$ reduction into renewable hydrocarbon fuel, Nanotechnology 28 (2017) 274002 8 pp..
[15] J. Jin, J.G. Yu, D.P. Guo, C. Cui, W.K. Ho, A hierarchical Z-scheme CdS-WO$_3$ photocatalyst with enhanced CO$_2$ reduction activity, Small 11 (2015) 5262–5271.
[16] J.Q. Yan, H. Wu, H. Chen, Y.X. Zhang, F.X. Zhang, S.F. Liu, Fabrication of TiO$_2$/C$_3$N$_4$ heterostructure for enhanced photocatalytic Z-scheme overall water splitting, Appl. Catal. B 191 (2016) 130–137.
[17] H.Y. Li, Y.J. Sun, B. Cai, S.Y. Gan, D.X. Han, L. Niu, T.S. Wu, Hierarchically Z-scheme photocatalyst of Ag@AgCl decorated on BiVO$_4$ (040) with enhancing photoelectrochemical and photocatalytic performance, Appl. Catal. B 170 (2015) 206–214.
[18] C.D. Song, X. Wang, J. Zhang, X.B. Chen, C. Li, Enhanced performance of direct Z-scheme CuS-WO$_3$ system towards photocatalytic decomposition of organic pollutants under visible light, Appl. Surf. Sci. 425 (2017) 788–795.
[19] J. Pan, G. Liu, G.M. Lu, H.M. Cheng, On the true photoreactivity order of {001}, {010}, and {101} facets of anatase TiO$_2$ crystals, Angew. Chem. Int. Ed. 50 (2011) 2133–2137.
[20] L.L. Wang, J. Ge, A.L. Wang, M.S. Deng, X.J. Wang, S. Bai, R. Li, J. Jiang, Q. Zhang, Y. Luo, Y.J. Xiong, Designing p-type semiconductor-metal hybrid structures for improved photocatalysis, Angew. Chem. Int. Ed. 53 (2014) 5107–5111.
[21] Y. Zhang, B. Deng, T.R. Zhang, D.M. Gao, A.W. Xu, Shape effects of Cu$_2$O polyhedral microcrystals on photocatalytic activity, J. Phys. Chem. C 114 (2010) 5073–5079.
[22] R.G. Li, H.X. Han, F.X. Zhang, D.G. Wang, C. Li, Highly efficient photocatalysts constructed by rational assembly of dual-cocatalysts separately on different facets of BiVO$_4$, Energy Environ. Sci. 7 (2014) 1369–1376.
[23] L.L. Zhang, W.H. Feng, B. Wang, K.Q. Wang, F. Gao, Y. Zhao, P. Liu, Construction of dual-channel for optimizing Z-scheme photocatalytic system, Appl. Catal. B 212 (2017) 80–88.
[24] S.Y. Bao, Q.F. Wu, S.Z. Chang, B.Z. Tian, J.L. Zhang, Z-scheme CdS-Au-BiVO$_4$ with enhanced photocatalytic activity for organic contaminant decomposition, Catal. Sci. Technol. 7 (2017) 124–132.
[25] S. Yu, Y.H. Kim, S.Y. Lee, H.D. Song, J. Yi, Hot-electron-transfer enhancement for the efficient energy conversion of visible light, Angew. Chem. Int. Ed. 53 (2014) 11203–11207.
[26] H.F. Li, H.T. Yu, X. Quan, S. Chen, H.M. Zhao, Improved photocatalytic performance of heterojunction by controlling the contact facet: high electron transfer capacity between TiO$_2$ and the {110} facet of BiVO$_4$ caused by suitable energy band alignment, Adv. Funct. Mater. 25 (2015) 3074–3080.
[27] S. Kohtani, J. Hiro, N. Yamamoto, A. Kudo, K. Tokumura, R. Nakagaki, Adsorptive and photocatalytic properties of Ag-loaded BiVO$_4$ on the degradation of 4-n-alkylphenols under visible light irradiation, Catal. Commun. 6 (2005) 185–189.
[28] R.F. Tong, C. Liu, Z.K. Xu, Q. Kuang, Z.X. Xie, L.S. Zheng, Efficiently enhancing visible light photocatalytic activity of faceted TiO$_2$ nanocrystals by synergistic effects of core-shell structured Au@CdS nanoparticles and their selective deposition, ACS Appl. Mater. Interfaces 8 (2016) 21326–21333.
[29] Y. Liu, P. Zhang, B.Z. Tian, J.L. Zhang, Core-shell structural CdS@SnO$_2$ nanorods with excellent visible-light photocatalytic activity for the selective oxidation of benzyl alcohol to benzaldehyde, ACS Appl. Mater. Interfaces 7 (2015) 13849–13858.
[30] W.B. Li, C. Feng, S.Y. Dai, J.G. Yue, F.X. Hua, H. Hou, Fabrication of sulfur-doped g-C$_3$N$_4$/Au/CdS Z-scheme photocatalyst to improve the photocatalytic performance under visible light, Appl. Catal. B 168 (2015) 465–471.
[31] M.P. Seah, L.S. Gilmore, G. Beamson, XPS: binding energy calibration of electron spectrometers 5-re-evaluation of the reference energies, Surf. Interface Anal. 26 (1998) 642–649.
[32] T.D. Thomas, P. Weightman, Valence electronic-structure of AuZn and AuMg alloys derived from a new way of analyzing auger-parameter shifts, Phys. Rev. B 33 (1986) 5406–5413.
[33] S. Anandan, N. Ohashi, M. Miyauchi, ZnO-based visible-light photocatalyst bandgap engineering and multi-electron reduction by co-catalyst, Appl. Catal. B 100 (2010) 502–509.
[34] S. Linic, P. Christopher, D.B. Ingram, Plasmonic-metal nanostructures for efficient conversion of solar to chemical energy, Nat. Mater. 10 (2011) 911–921.
[35] M. Kim, Y.K. Kim, S.K. Lim, S. Kim, S.I. In, Efficient visible light-induced H$_2$ production by Au@CdS/TiO$_2$ nanofibers: synergistic effect of core-shell structured Au@CdS and densely packed TiO$_2$ nanoparticles, Appl. Catal. B 166 (2015) 423–431.
[36] D.A. Armstrong, R.E. Huie, W.H. Koppenol, S.V. Lymar, G. Merenyi, P. Neta, B. Ruscic, D.M. Stanbury, S. Steenken, P. Wardman, Standard electrode potentials involving radicals in aqueous solution: inorganic radicals (IUPAC technical report), Pure. Appl. Chem. 87 (2015) 1139–1150.
[37] J.L. Wang, Y. Yu, L.Z. Zhang, Highly efficient photocatalytic removal of sodium pentachlorophenate with Bi$_3$O$_4$Br under visible light, Appl. Catal. B 136 (2013) 112–121.